ARTICLES

Mass-identified particle production in proton-antiproton collisions at $\sqrt{s} = 300$, 540, 1000, and 1800 GeV

T. Alexopoulos,[7] C. Allen,[6,*] E. W. Anderson,[4] V. Balamurali,[5] S. Banerjee,[5,3] P. D. Beery,[5,†] P Bhat,[3] J. M. Bishop,[5] N. N. Biswas,[5] A. Bujak,[6] D. D. Carmony,[6] T. Carter,[2,3] Y. Choi,[6,‡] P. Cole,[6,§] R. DeBonte,[6] V. DeCarlo,[1] A. R. Erwin,[7] C. Findeisen,[7,‖] A. T. Goshaw,[2] L. J. Gutay,[6] A. S. Hirsch,[6] C. Hojvat,[3] J. R. Jennings,[7] V. P. Kenney,[5] C. S. Lindsey,[4,3] C. Loomis,[2] J. M. LoSecco,[5] T. McMahon,[6] A. P. McManus,[5,¶] N. Morgan,[6,**] K. Nelson,[7,¶] S. H. Oh,[2] N. T. Porile,[6] D. Reeves,[3,††] A. Rimai,[6] W. J. Robertson,[2] R. P. Scharenberg,[6] S. R. Stampke,[5,‡‡] B. C. Stringfellow,[6] M. Thompson,[7] F. Turkot,[3] W. D. Walker,[2] C. H. Wang,[4,2] J. Warchol,[5] D. K. Wesson,[3,§§] and Y. Zhan[5,‖‖]

(E735 Collaboration)

[1]*Department of Physics, DePauw University, Greencastle, Indiana 46135*
[2]*Department of Physics, Duke University, Durham, North Carolina 22706*
[3]*Fermi National Accelerator Laboratory, P.O. Box 500, Batavia, Illinois 60510*
[4]*Department of Physics, Iowa State University, Ames, Iowa 50011*
[5]*Department of Physics, University of Notre Dame, Notre Dame, Indiana 46556*
[6]*Departments of Physics and Chemistry, Purdue University, W. Lafayette, Indiana 47907*
[7]*Department of Physics, University of Wisconsin, Madison, Wisconsin 53706*

(Received 21 September 1992)

The yields and average transverse momenta of pions, kaons, and antiprotons produced at the Fermilab $\bar{p}p$ collider at $\sqrt{s} = 300$, 540, 1000, and 1800 GeV are presented and compared with data from the energies reached at the CERN collider. We also present data on the dependence of average transverse momentum $\langle p_t \rangle$ and particle ratios as a function of charged particle density $dN_c/d\eta$; data for particle densities as high as six times the average value, corresponding to a Bjorken energy density 6 GeV/fm^3, are reported. These data are relevant to the search for quark-gluon phase of QCD.

PACS number(s): 13.85.Ni

I. INTRODUCTION

With the advent of Fermilab collider facilities, it has been feasible to study particle production in hadron-hadron collisions at the highest possible energy. Typically many hadrons are produced in high-energy collisions; the study of particle production in high multiplicity events is then particularly interesting to investigate the possibility of phase transition of hadronic matter to a deconfined quark-gluon plasma [1]. In this context, energy densities above 2 GeV/fm^3 are thought to be required.

We report here results on particle production in $\bar{p}p$ collisions from Experiment E735 performed at the C0-intersection region of the Fermilab Tevatron Collider. In this experiment, we have studied the yields and the transverse momentum distributions of centrally produced $\pi^{\pm}$, $K^{\pm}$, p, and $\bar{p}$.

The experiment was run during the 1988–1989 Tevatron running period, primarily collecting data triggered to enrich high multiplicity events in $\bar{p}p$ interaction at a center-of-mass energy $\sqrt{s} = 1800$ GeV. The present data sample has been collected with the same apparatus, including minor upgrades, as utilized for results published previously [2,3]. With the present experimental setup, data were also taken at the collider energy of $\sqrt{s} = 300$, 540, and 1000 GeV.

In this paper we present results on $\pi^{\pm}$, $K^{\pm}$, and $p/\bar{p}$

*Now at University of Texas, Austin, TX 78712-1081.
†Now at University of California, Riverside, CA 92521.
‡Now at Sungkyunkwan University, Suwon, Republic of Korea.
§Now at George Washington University, Washington, D.C. 20052.
‖Now at University of Zürich, Zürich, Switzerland.
¶Now at University of Virginia, Charlottesville, VA 22901.
**Now at Virginia Polytechnic Institute, Blacksburg, VA 24061.
††Now at 9735 St. Augustine Rd., Jacksonville, FL 32257.
‡‡Now at SSCL, Dallas, TX 75237.
§§Now at University of Massachusetts, Amherst, MA 01003.
‖‖Now at System Resources Consulting, Inc., Oakbrook, IL 60481.

 ©1993 The American Physical Society

production to study their energy dependence using data at $\sqrt{s}=300$, 540, 1000, and 1800 GeV. Using the high statistics data at $\sqrt{s}=1800$ GeV, a detailed study of the dependence of particle production on event multiplicity is also presented here. Events with more than 300 produced hadrons have been studied; the Bjorken estimate for the energy density [4] in such events is 6 GeV/fm^3. These data have recently been utilized to study the production of Λ and other hyperons [5].

The paper is organized as follows. In Secs. II and III we describe the experimental setup and data reduction procedure, respectively. We present event selection criteria in Sec. IV. In Sec. V we discuss biases and acceptance of the detectors. In Sec. VI we outline the procedure for evaluating transverse momentum distributions of mass-separated particles. Section VII A deals with the energy dependence of $\langle p_t \rangle$ and particle ratios using "minimum bias" events of four different collider energies. In Sec. VII B we study particle ratios and $\langle p_t \rangle$ as a function of particle density $dN_c/d\eta$, using high statistics sample of high multiplicity events at $\sqrt{s}=1800$ GeV. We summarize our results in Sec. VIII.

II. EXPERIMENTAL SETUP

Details of the experimental arrangement and the performance of the apparatus have been reported earlier [6–14]. Here we briefly sketch the experimental layout. The experiment measures the overall multiplicity of events using an array of scintillation detectors and a central tracking chamber. A single arm magnetic spectrometer at polar angle $\theta=90°$ along with a time-of-flight (TOF) system samples the particle spectra of the centrally produced particles. The E735 experimental setup is shown in Fig. 1.

The multiplicity hodoscope consists of 240 scintillation counters surrounding the collision region and covers $-3.25<\eta<+3.25$ in pseudorapidity and $0°<\phi<360°$ in azimuth angle. The system consists of a central barrel hodoscope covering the range $-1.64<\eta<+1.64$ with 48 counters for each of the positive and negative pseudorapidity regions. The two end cap hodoscopes each consist of three rings (each ring has 24 counters), extending the pseudorapidity coverage to -3.25 on one side and to $+3.25$ on the other side. These 240 scintillators are instrumented to make pulse height and time measurement [7,13].

The particles hitting the barrel scintillator hodoscope are also detected in a cylindrically symmetric drift chamber which covers the pseudorapidity interval $-1.6<\eta<+1.6$. This central tracking chamber (CTC) samples the charged multiplicity of events for about 10% of the triggered events. The technical details of chamber construction and track reconstruction procedure are described elsewhere [6,11].

The spectrometer arm approximately covers the pseudorapidity range $-0.36<\eta<1.0$ with an azimuthal acceptance of $18°(0°<\phi<18°)$ subtending a solid angle of about 0.32 sr. For the location of the vertex of the $\bar{p}p$ interaction along the beam line (z direction taken as positive along the proton direction), a 1 m long low-mass mini drift chamber [9,12] comprised of three planes is placed at 14 cm from the beam line, just outside the 3-mm-thick aluminum vacuum pipe wall (located at 12 cm from the beam) and inside the CTC (22 cm inner radius). A dipole magnet with its center placed at $x=75$ cm provides a 50 MeV/c transverse momentum kick. Particle trajectories are measured by four planes of "premagnet" and four planes of "postmagnet" drift chambers [9,12] covering the magnet aperture. These chambers are fol-

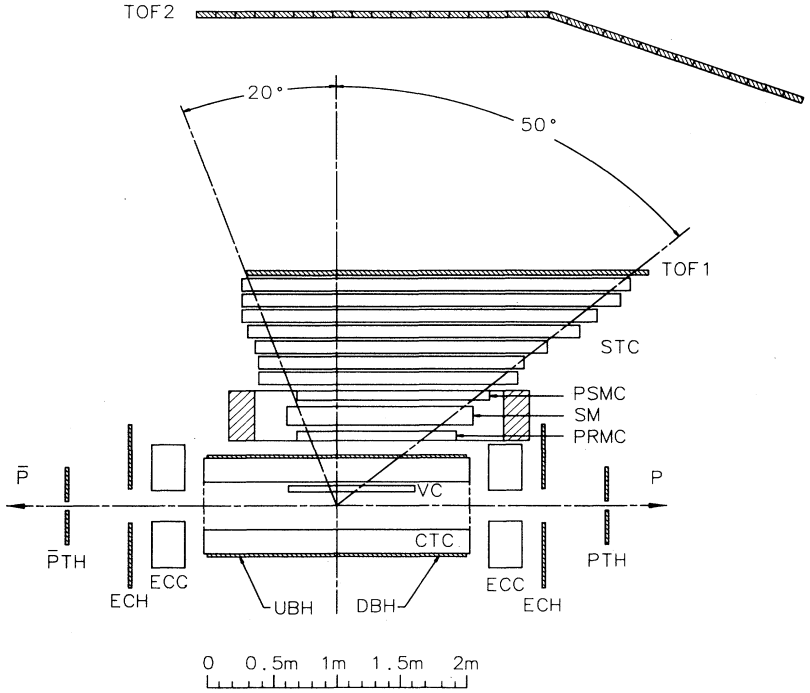

FIG. 1. Plan view of E735 experimental setup. The legends shown are as follows. P̄TH: antiproton trigger hodoscope; ECH: end-cap hodoscope; ECC: end-cap chambers; UBH: upstream barrel hodoscope; DNH: downstream barrel hodoscope; PTH: proton trigger hodoscope; CTC: central tracking chamber; VC: vertex chamber; PRMC: premagnet chamber; SM: spectrometer magnet; PSMC: postmagnet chamber; STC: straw-tube chambers; TOF1: time-of-flight No. 1 hodoscope; TOF2: time-of-flight No. 2 hodoscope.

lowed by 14 planes of straw-tube drift chambers [8], 6 of which are used for stereo views (stereo angle $=4°$).

Behind the straw chambers, there are two scintillator hodoscopes (TOF1 and TOF2), TOF1 at 2 m consisting of 7 horizontal counters and TOF2 at 4 m consisting of 32 vertical counters to measure the time of flight of particles in the spectrometer arm [10]. These two TOF arrays play complementary roles in π-K separation; the 2m TOF1 is more effective in the identification of low-momentum kaons which decay before reaching the 4 m TOF2, while the 4 m TOF2 is more effective in resolving high-momentum K's and π's.

The time-of-flight measurement involves two other hodoscopes which are placed just outside end caps of the multiplicity hodoscope detecting particles produced at small angles with respect to the beam directions (pseudorapidity range $3.0 \leq |\eta| < 4,5$). There are 15 counters in each of these hodoscopes. The timing information from these counters is used in the trigger logic by imposing timing windows appropriate for the arrival of at least one fast particle in each of these hodoscopes from beam-beam interaction time. These data are used off line for determining precise interaction time and the interaction vertex along the beam direction, and for rejecting background events.

III. DATA REDUCTION

Using the time-of-flight information from the TOF hodoscopes placed in the beam directions, the vertex z position of beam-beam interaction point is determined for each triggered event. A more precise z vertex is obtained for events having one or more tracks in the spectrometer arm by extrapolating the tracks to $x=0$ beam constraint.

The number of hits N_h, observed in the multiplicity hodoscopes (barrel plus two end caps), is the raw data associated with the overall multiplicity of an event. Since the central tracking chamber (CTC) and the barrel scintillator hodoscope cover the same pseudorapidity range, the number of hits in the barrel hodoscope can be compared with the number of tracks reconstructed in the CTC ($N_{\rm CTC}$). However, since there is only a finite number of counters (i.e., 96) in the barrel, saturation effects are observed due to the probability that more than one particle traverses the same counter.

In the spectrometer arm, the track reconstruction program starts by associating hits in the straw chambers behind the magnet with tracks. These are then traced back through the magnet to match with hits in the "post-magnet" and "premagnet" chambers to determine their momenta. Tracks are rejected if the momentum is less than 150 MeV/c, since the reconstruction efficiency is poor in this region. In the accepted momentum region, we estimate that the track reconstruction efficiency is about 95%, which depends on the sign of the charge of particles only at low momenta [2,11]. At $p=150$ MeV/c the efficiency is about 83 (64%) for negative (positive) particles. The momentum resolution [2,12] of the spectrometer is dictated by multiple scattering and the wire chamber measurement resolution, and can be expressed as

$$dp/p = \sqrt{(0.04p)^2+(0.04/\beta)^2}\ , \tag{1}$$

where p is the momentum in GeV/c, and β is the particle velocity.

The pulse heights recorded in TOF counters are used to make "time-slewing" corrections [10] for the time-to-digital-converter (TDC) values from these counters. Using corrected time measurements from both ends of a counter, the hit position (z value at TOF1 plane, and y value at TOF2 plane) and the time-of-flight of a particle going through the spectrometer are calculated. The hit position in a counter (for example, in TOF2 hodoscope) is given by

$$y = \tfrac{1}{2}[L - v(t_2 - t_1)]\ , \tag{2}$$

where v is the velocity of light propagation in the scintillator, L is the length of the counter, and t_2 and t_1 are the TDC values from each end of the counter. The time of flight with respect to a start Tevatron clock is given by

$$t' = \tfrac{1}{2}[(t_1+t_2)-(L/v)]\ . \tag{3}$$

The actual time of flight is obtained as

$$t = t' - t_0\ , \tag{4}$$

where t_0 is the beam-beam interaction time as discussed below. We note that these relations are only valid if the counter is hit by one and only one particle. Using the tracking information in the spectrometer arm, we reject TOF1 and/or TOF2 data if a counter in these hodoscopes is multiply hit.

The time-of-flight information from the trigger hodoscopes is used to determine the collision point (z vertex) and time of beam-beam interaction. If T_1 is the time given by a counter from the trigger hodoscope placed at $z=d=2m$, and T_2 is the time from a counter in the trigger hodoscope at $z=-2$ m, then the z vertex of the event is given by

$$z_{\rm ev} = \tfrac{1}{2}c(T_2 - T_1) \tag{5}$$

assuming that the particles produced at small angles with respect to the beam direction travel with velocity c. The event occurrence time with respect to the Tevatron clock is

$$t_0 = \tfrac{1}{2}[(T_1+T_2)-(2d/c)]\ . \tag{6}$$

Again these relations strictly hold when a counter is hit by one and only one particle. We, however, cannot check this since there are no tracking detectors which cover the geometry of these hodoscopes. Multiple hits will introduce an error in t_0 determination and hence also in the time-of-flight measurement for particles in the spectrometer arm. The segmentation of these hodoscopes are such that the probability of multiple hits in a counter is negligible for low and medium multiplicity events. For very high multiplicity events, however, this effect results in the loss of mass resolution for particle identification. This topic will be further discussed in Sec. VI, where we will also mention the corrections involved in high multiplicity events.

IV. EVENT AND TRACK SELECTION CRITERIA

An event is recorded if hits are detected in both trigger hodoscopes within the beam crossing time. These events constitute our "minimum-bias" sample. High multiplicity events are enhanced with an on-line trigger processor utilizing signals from the multiplicity hodoscope and scaling events in different multiplicity regions.

The bias of the data due to the occurrence of multiple interactions per bunch crossing can be neglected. The overall probability of two events occurring in a single beam crossing, at the highest luminosity in the C0 intersection region, is estimated to be 0.2%. The probability that the highest multiplicity events be associated with a second event in the same crossing is estimated to be 2%.

A. Event selection

To study the background ("beam-gas" interactions inside the beam pipe, beam interaction with the wall of the pipe, etc.) for the triggered events, data were collected for events satisfying the trigger condition when one or more antiproton bunches were missing in the collider. The events obtained with the proton bunch crossing the interaction region in the absence of the corresponding antiproton bunch are considered to be representative of the background ("background" sample). In order to remove the backgrounds, the following cuts are imposed on the data [11–14].

(a) The beam-beam events are required to satisfy $N_p > 1$ and $N_{\bar{p}} > 1$, where N_p and $N_{\bar{p}}$ are the number of hits in the upstream (relative to the proton beam direction) and downstream trigger hodoscope, respectively. In Fig. 2 we compare the hit distributions in these hodoscopes for beam-beam data with the background data which are dominantly populated by $N_p, N_{\bar{p}} \leq 1$.

(b) The event vertex z_{ev}, calculated using the time information from the trigger hodoscope, is required to be within a fiducial region $-40 < z_{ev} < 60$ cm in order to contain the event within the detector system.

(c) The background contribution in high multiplicity events is also apparent from the study of the upstream-downstream asymmetry A of hits in end cap multiplicity hodoscopes:

$$A = (N_u - N_d)/(N_u + N_d) , \tag{7}$$

where N_u and N_d are the number of hits in the upstream and downstream multiplicity hodoscope, respectively. Figure 3 shows this asymmetry distribution for minimum-bias triggers with $N_h > 80$. Events with $|A| < 0.6$ are expected from $\bar{p}p$ interactions and are classified as such. The highly asymmetric events ($|A| > 0.6$) appear to be beam-gas events or background.

(d) The time information from the end-cap multiplicity hodoscopes is also used for background elimination. For $\bar{p}p$ events, the hit time of the upstream end-cap counter should be correlated to the hit time of the downstream end-cap counter. The uncorrelated events, which seem to occur outside the E735 detector region or between the region defined by trigger and end-cap hodoscopes, are removed.

The multiplicity distribution of the triggered data with no missing bunches, after applying these cuts, is shown in Fig. 4. In this figure we also show the multiplicity distribution for the missing bunch background events after the same cuts and normalizing these data to correspond to the no missing bunch sample. From this plot, we estimate that the overall selected events contain less than 2%

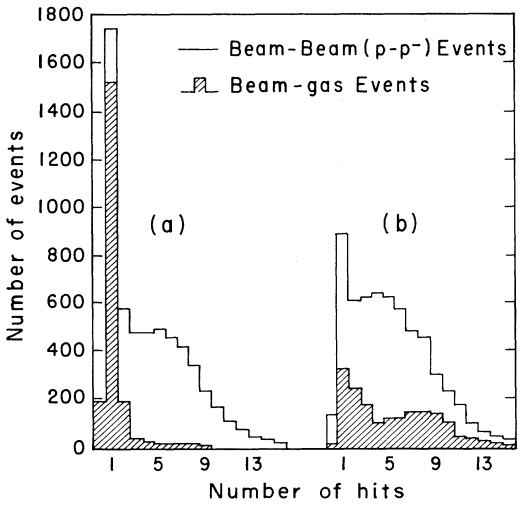

FIG. 2. Distribution of the number of hits in (a) the upstream and (b) downstream trigger hodoscopes for two classes of triggered events: beam-gas events (hatched) associated with only the proton beam in the Tevatron and beam-beam events associated with both proton and antiproton beams in the Tevatron. (Note that beam-beam events intrinsically contain beam-gas events as backgrounds.)

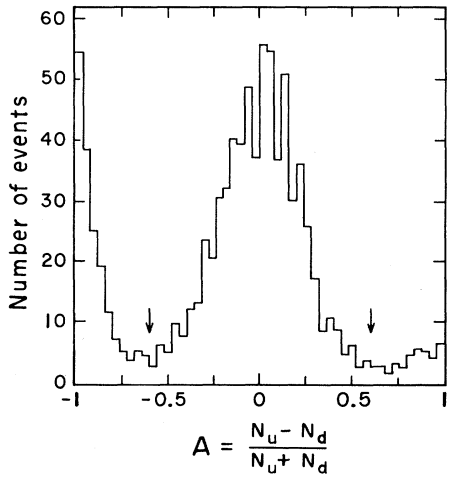

FIG. 3. Distribution of asymmetry A calculated from the number of hits observed in upstream and downstream end-cap multiplicity hodoscopes for events associated with proton-antiproton bunches triggered as "minimum-bias" events with $N_h > 80$. The events with $|A| < 0.6$ are classified as beam-beam interaction events. The same distribution for proton bunch only (not shown) is peaked at $A = -1$, and mostly populated in the $A < -0.6$ region (beam-gas events).

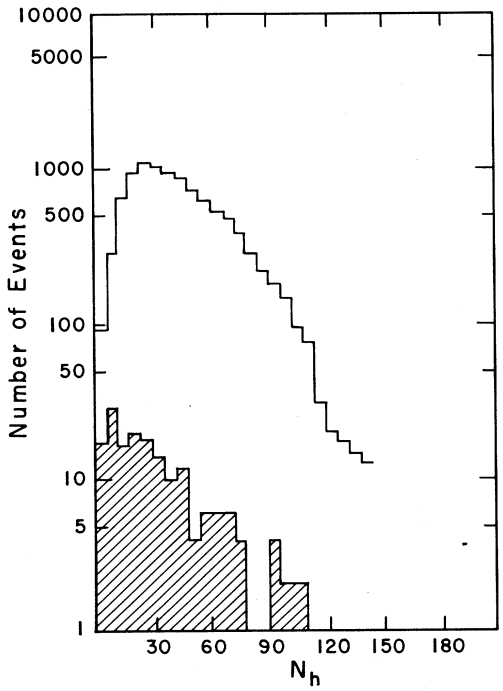

FIG. 4. Distribution of number of hits, N_h in the multiplicity hodoscope after applying cuts (see text) for two classes of triggers: beam-beam events associated with proton-antiproton bunches, and beam-gas events associated with only the proton bunch in the Tevatron. The distribution for beam-gas events (shown hatched) is our estimate for the background in beam-beam event distribution.

background events. The background contribution, however, depends on multiplicity ($\sim 10\%$ at $N_h = 120$).

B. Track selection

The events selected with the criteria mentioned above and associated with 1 or more tracks in the spectrometer arm are used for the study of particle momentum distributions. Poorly reconstructed and background tracks are rejected, (a) if the fitted momentum is less than 150 MeV/c (these low-momenta tracks have poorly reconstructed efficiency), (b) if χ^2 per degree of freedom is greater than 3, (c) if the fitted momentum error is greater than 2 standard deviations from the expected error [Eq. (1)]; (d) if the track y intercept at the beam line ($x = 0$) is outside ± 10 cm (due to the y resolution of the spectrometer arm), (e) if the beam-beam interaction point (z_{ev}) obtained from the trigger hodoscope does not agree with the track intercept, z_T at the beam line ($x = 0$), i.e., if $|z_{ev} - z_T| > 10$ cm (the rms error in z is ~ 4 cm), and (f) for more than 1 track in the spectrometer arm surviving the cuts mentioned so far, if the difference in z_T values of any pair of tracks i, j,

$$|z_T(i) - z_T(j) > 2.0 \text{ cm}$$

and if their average value of

$$\langle z_T \rangle (\text{av}) = [z_T(i) + z_T(j)]/2$$

does not agree with the event vertex by

$$|z_{ev} - \langle z_T \rangle| > 10.0 \text{ cm} .$$

C. TOF-data selection

As described in the previous section, the timing information from TOF counters yields the hit position of a particle traversing the spectometer. These data are compared with the values given by the track reconstruction program to apply a cut as described below. We note here that the pulse heights recorded in TOF counters were not a useful indicator of multiple hits in a given counter.

The accepted tracks in the spectrometer arm are extrapolated to x positions of TOF1 and TOF2 to predict the y, z positions of hits in these hodoscopes. Criteria used for track selection in the comparison of the predicted positions with those from the time-of-flight measurement, are as follows.

(a) For TOF1, the difference between the z values must be less than 10 cm. Since TOF1 is segmented in the y direction (width $= 15$ cm), we require that the counter predicted to be hit by track extrapolation is the one which is actually hit or an adjacent one.

(b) For TOF2, segmented in z direction (width $= 10$ cm), we accept tracks if the counter predicted to be hit is the one which is actually hit or an adjacent one. The y resolution in track reconstruction (small stereo angle) does not allow us to impose constraint on the y position determined by TOF2.

(c) If two or more tracks hit the same counter, the tracks are rejected for time-of-flight analysis.

V. BIAS, ACCEPTANCE OF EXPERIMENTAL DATA

The physics analysis is based on 4.2 million events. Starting with 12.2 million triggered events, the sample was reduced to 8.2 million after background subtraction and rejection of events with no tracks in the spectrometer arm. The track quality cuts and TOF selection then reduce the sample to 4.2 million, with 92.7%, 2.3%, 3.8%, and 1.2% at $\sqrt{s} = 1800$, 1000, 540, and 300, respectively. From Monte Carlo studies we have evaluated detection efficiencies of our experimental setup.

A. Trigger bias

We have used UA5 [15] and ISAJET [16] event generators to produce nonsingle diffractive events as input to GEANT program to simulate the trigger system. The trigger efficiency as a function of hodoscope multiplicity is plotted in Fig. 5. The efficiency is low only at very low multiplicity, reaching a value of 90% at $N_h \sim 30$. Our efficiency curve is insensitive to whether we use UA5 or ISAJET generator. The trigger bias is taken into account whenever data are summed over all multiplicities.

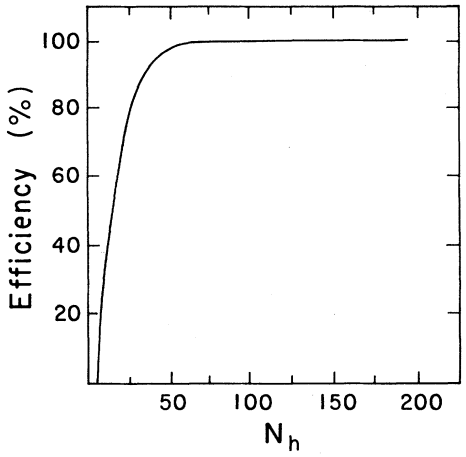

FIG. 5. Plot of trigger efficiency as a function of hodoscope multiplicity N_h.

B. Multiplicity calculation

The total multiplicity of an event is related to the number of hits N_h observed in the multiplicity hodoscope which is segmented into 240 scintillating counters. The determination of the relation between the true charged multiplicity and the hodoscope hit multiplicity has been done by Monte Carlo method [13]. The conversion from the measured number of hits N_h, to the true charged multiplicity N_C has been empirically parametrized as

$$N_C = 0.875N_h - 0.608\times10^{-3}N_h^2 + 0.141\times10^{-4}N_h^3 \ . \quad (8)$$

As discussed earlier, the number of hits in the barrel multiplicity hodoscope can be checked against the number of tracks reconstructed in the central tracking chamber (CTC) in $\sim 10\%$ of the events.

The Monte Carlo calculation also provides us with the expected correlation between the number of tracks in the spectrometer arm, N_s, and hodoscope hit multiplicity N_h. In Fig. 6, we show these correlations for the actual data and compare them with the Monte Carlo calculation [2]. There is good agreement between data and the Monte Carlo.

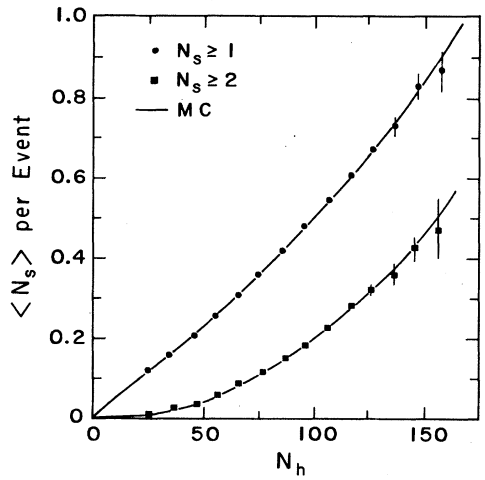

FIG. 6. Plot of the average number of tracks $\langle N_s \rangle$ in the spectrometer arm (after track cuts, see text) as a function of N_h, the number of hits in the multiplicity hodoscope. $\langle N_s \rangle$ has been separately calculated by summing N_s for events with $N_s \geq 1$ and for events with $N_s \geq 2$ (divided by the total number of events including those with $N_s = 0$). The curves obtained from a Monte Carlo calculation (see text) are shown for comparison with the data.

C. Spectrometer acceptance

In order to calculate the transverse momentum (p_t) spectra and the ratio of particles, acceptance curves for different particles are obtained by a Monte Carlo simulation [14] utilizing the program GEANT. Particles of a given type fixed within a narrow p_t interval are generated uniformly in azimuth ($-5° < \phi < 25°$) and within the rapidity $-2.0 < y < 2.0$ using the same event z-vertex distribution as the real data. The particles and their decay products are followed through the spectrometer detector material and hits are generated including multiple scattering, energy loss, and the measured detector position resolution. The simulated detector hits are input to the reconstruction program that is used for the real data analysis. The reconstructed tracks are then subjected to the same cuts as used in the real data. The acceptance, calculated as the ratio of the number of good tracks to the number of Monte Carlo tracks, is determined as a function of p_t and particle type. The acceptances as a function of p_t are shown in Fig. 7 for $\pi^{\pm}$, $K^{\pm}$, $p/\bar{p}$; these curves correspond to the case where we have set acceptance to be 1 for π^+ particles at $p_t = 3.0$ GeV/c.

D. Time-of-flight resolution and mass distribution

In our Monte Carlo data discussed above, the time of flight for each particle is also recorded. The actual time of flight obtained from tracking a particle to the counter array is smeared by Gaussian distribution with time resolutions, $\sigma = 140$ ps for event occurrence time t_0, $\sigma = 170$

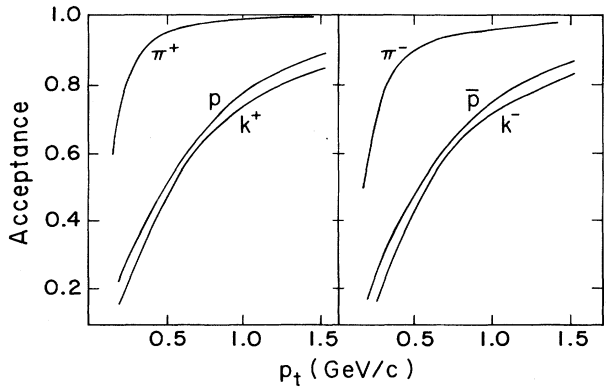

FIG. 7. Acceptance curves for positively and negatively charged particles as a function of p_t as calculated by Monte Carlo method (see text).

ps for TOF1 time of flight, and $\sigma = 160$ ps for TOF2 time of flight t [10]. Mass-squared distributions of Monte Carlo events using three equal π^-, K^-, and $\bar{p}$ samples as input are shown in Figs. 8(a) and 8(b) for p_t intervals $0.4 < p < 0.5$ GeV/c (TOF1 data) and $1.15 < p_t < 1.35$ GeV/c (TOF2 data), respectively. These distributions reproduce the peaks and the width of M^2 distributions of experimental data shown in Figs. 9(a) (TOF1 data) and 9(b) (TOF2 data). We note that σ used for all particle types and all p_t is the same as in Figs. 8(a) and 8(b). The variation of widths of mass peaks in Fig. 8 as a function of M^2 and p_t results from the convolution of momentum resolution, decay, and secondary interaction effects.

VI. DETERMINATION OF TRANSVERSE MOMENTUM SPECTRA OF PARTICLES

From the measured mass-squared (M^2) distributions the individual $\pi^\pm$, $K^\pm$, and $p/\bar{p}$ contributions must be extracted. The M^2 distributions [see Figs. 9(a) and 9(b)] show clear π, K, and $p/\bar{p}$ peaks for TOF1 (at 2 m) data and for TOF2 (at 4 m) data. We select $-0.14 < M^2 < 0.16$ GeV^2 as the pion mass region, $0.16 < M^2 < 0.36$ GeV^2 as the K mass region and $0.5 < M^2 < 1.4$ GeV^2 as the mass region for $p/\bar{p}$, to obtain pion, kaon, and $p/\bar{p}$ signals, n_π, n_K, and n_p for negative- and positive-charged particles separately. We determine these quantities as a function of p_t by subdividing the data in several p_t intervals. (In Fig. 9, we have illustrated data for two such p_t intervals.)

The Monte Carlo generated M^2 distributions [see Figs. 8(a) and 8(b)] are utilized to construct an "efficiency matrix" accounting for the combined effects of spectrometer acceptance, track reconstruction efficiency, and the cuts imposed on the data. The efficiency matrix (determined as a function of p_t, mass, and charge of particles) relates the experimentally observed data n_π, n_K, and n_p to the corresponding corrected values N_π, N_K, and N_p as follows:

$$\begin{bmatrix} n_\pi \\ n_K \\ n_p \end{bmatrix} = \begin{bmatrix} e_{\pi\pi} & e_{\pi K} & e_{\pi p} \\ e_{K\pi} & e_{KK} & e_{Kp} \\ e_{p\pi} & e_{pK} & e_{pp} \end{bmatrix} \begin{bmatrix} N_\pi \\ N_K \\ N_p \end{bmatrix} . \tag{9}$$

Here $e_{\pi\pi}$, $e_{\pi K}$, and $e_{\pi p}$ are obtained by counting the numbers of events from the pion sample of the Monte Carlo data in the mass regions used in defining pion, kaon, and p signals, and then dividing these numbers by the number of generated events. Similarly, $e_{K\pi}$, e_{KK}, and e_{Kp} are evaluated from kaon Monte Carlo events, and $e_{p\pi}$, e_{pK}, and e_{pp} from $p/\bar{p}$ Monte Carlo data. For a given p_t, mass and charge, two different efficiency matrices, one for

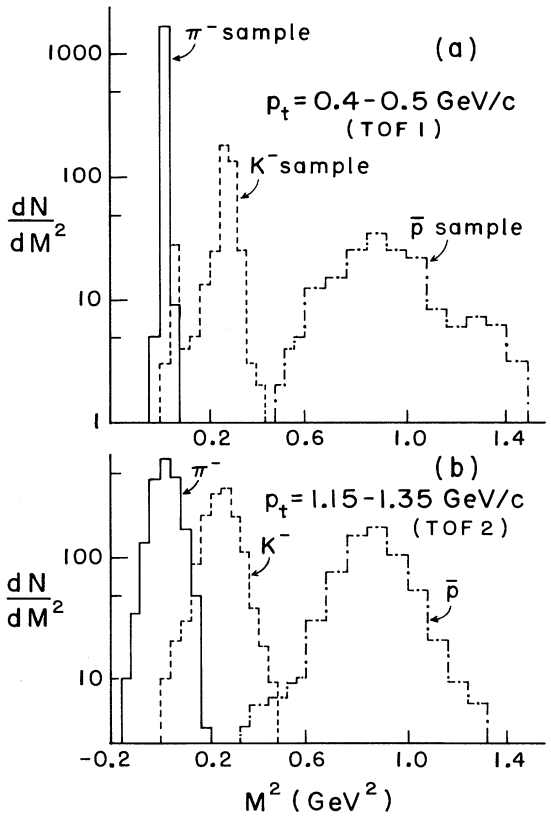

FIG. 8. Mass-squared distributions of Monte Carlo events (a) from TOF1 for p_t interval $0.4 < p_t < 0.5$ GeV/c using three equal π^-, K^-, and $\bar{p}$ samples as input; (b) the same as in (a) but from TOF2 for p_t interval $1.15 < p_t < 1.35$ GeV/c.

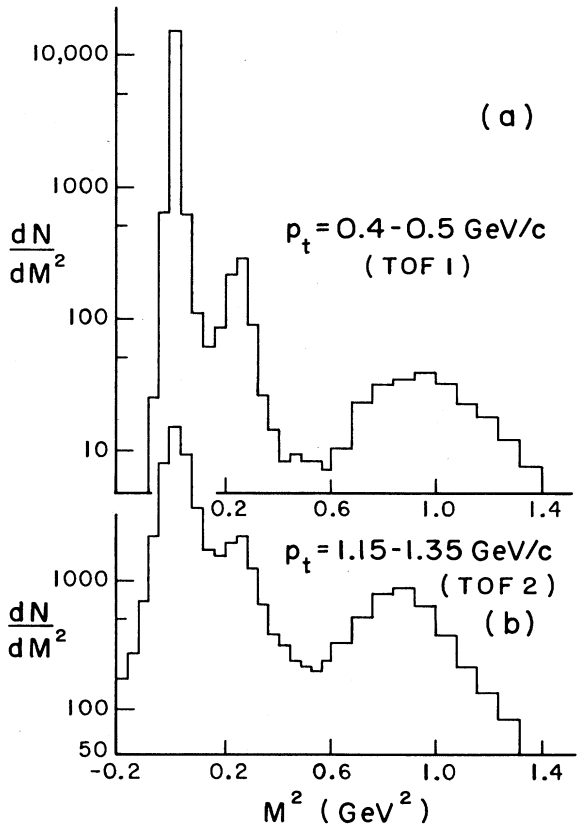

FIG. 9. Mass-squared distribution of the spectrometer data (a) for p_t interval $0.4 < p_t < 0.5$ GeV/c (TOF1) and (b) for p_t interval $1.15 < p_t < 1.35$ GeV/c (TOF2).

TOF1 and the other for TOF2, have been determined. We note, as mentioned in a previous section, that the mass-squared distributions for Monte Carlo data replicate the same distributions of the experimental data and that we impose the same M^2 cut in both cases to extract signals for various particles.

The p_t dependence of the diagonal elements of the efficiency matrix can be seen in Figs. 7(a) and 7(b). The off-diagonal elements are negligible at low P_t where the mass peaks are well separated but become more significant for higher p_t region.

We have also investigated [11,14] the dependence of the matrix on the charged multiplicity of the events. We have generated samples of events having $N_C=45$, 145, 165, 195, and 255 (over 4π solid angle) according to UA5 generator, closely resembling the data in terms of single-particle p_t and y distributions as well as in K/π and p/π ratios. The hits due to one or more tracks passing through the spectrometer after GEANT processing are replaced by hits from a fixed momentum particle of assigned mass. The event is then processed through the track reconstruction program to determine momenta of the particles in the spectrometer arm. The time of flight is determined from the expected flight time smearing it by the time resolution of TOF1/TOF2 and taking account of its shift due to t_0 signal derived from trigger hodoscopes (discussed in Sec. III). The efficiency matrix, evaluated for various multiplicities, show that our experimental setup affects detection efficiency at very high multiplicities (decreases $\sim 10\%$ from lowest to the highest multiplicity). When the multiplicity is high, the probability of more than one track (including secondary tracks) passing through the spectrometer increases, influencing track reconstruction efficiency. Also the occurrence of events with at least one counter in the trigger hodoscope having one and only one hit (to generate t_0 signal) decreases; this effect increases the probability that the time-of-flight measurement of some tracks are not so precise. Using multiplicity dependent efficiency, we have compensated these systematic effects in the data.

In fact, other independent studies have been performed to evaluate acceptance corrections for the data. In these studies, the overall acceptance has been factorized into geometrical and track reconstruction efficiencies which have been determined as a function of p_t, the particle type, and event multiplicity.

In one study [11], the PYTHIA event generator [17] is used to simulate the background as a function of multiplicity. The track reconstruction efficiency calculations involved a PYTHIA contribution for mimicking the event background on which a signal track was shuffled and the combined tracks are fed into the detector simulation program, which was based upon GEANT. Particle decays, em showers and energy loss of the particles were taken into account using a realistic representation of the geometry and material composition of the E-735 detectors. The particles are mass selected using the M^2 cuts mentioned earlier and the contribution of events outside the cut [called mass reconstruction efficiency (MRE)] is determined by fitting the mass-squared distribution with a Gaussian curve. The p_t distributions are then obtained by applying geometrical, track reconstruction efficiencies, and MRE.

In another study, we have attempted to estimate the background correction and mass reconstruction efficiency using experimental time-of-flight data as a consistency check. Since a given particle is detected by two TOF hodoscopes, the mass M_1, obtained from TOF1, should be correlated with M_2, the mass obtained from TOF2. In order to calculate the numbers of each type of particles using M_1 values, we evaluate the probability that a particle is a pion, kaon, and proton using the more precise value of mass M_2 given by the TOF2 system. Because of limited statistics, we choose four mass intervals: $M_1<0.3$ GeV, $0.30<M_1<0.37$ GeV, $0.37<M_1<0.7$ GeV, and $0.7<M_1<1.3$ GeV. The M_2 distributions for events in each of these M_1 intervals are plotted separately and the fraction of pions, kaons, and protons are then determined from these plots to obtain particle identification probabilities. This procedure has been done for every p_t bin of width 0.1 GeV/c to obtain p_t distributions.

We have compared the results obtained from three different analyses by fitting the corrected data to obtain $\langle p_t \rangle$ values and the particle ratios; from this comparison, we estimate systematic errors, which dominate over the statistical errors in the analysis of data presented in Sec. VIII. In Tables II(a) and II(b), we therefore present statistical and systematic errors separately.

Corrected p_t distributions are determined from the values of N_π, N_K, and N_p obtained by inverting the matrix Eq. (9). These distributions for positive and negative pions (kaons) agree and are averaged together. We observe an excess of p over $\bar{p}$ at low p_t ($0.03<p<0.6$ GeV/c) consistent with the higher background of secondary protons from interactions of pions with the material surrounding the beam-beam interaction region. We therefore present data on the production of $\bar{p}$ only.

The corrected p_t distributions, obtained by applying TOF1 and TOF2 efficiency matrices separately, agree with each other and are combined together. The resulting charged pion p_t distributions still contain an $e^\pm$ background from π^0 decay effects ($\sim 5\%$ overall) and $\pi^\pm$ background from K_s^0 decays ($\sim 8\%$ overall), which mostly affect the low p_t region [3]. The p_t distributions presented in this paper have been corrected for these backgrounds by estimating their effects from Monte Carlo calculation.

VII. PHYSICS RESULTS: PARTICLE RATIOS AND AVERAGE TRANSVERSE MOMENTUM

A. Energy dependence

The invariant distributions $d^2N/(dy\,dp_t^2)$ as a function of p_t are presented in Fig. 10 for the pion sample, in Fig. 11 for the kaon sample, and in Fig. 12 for the $\bar{p}$ data. In each of these figures, we have shown data for four energy values, $\sqrt{s}=300$, 540, 1000, and 1800 GeV. The kaon

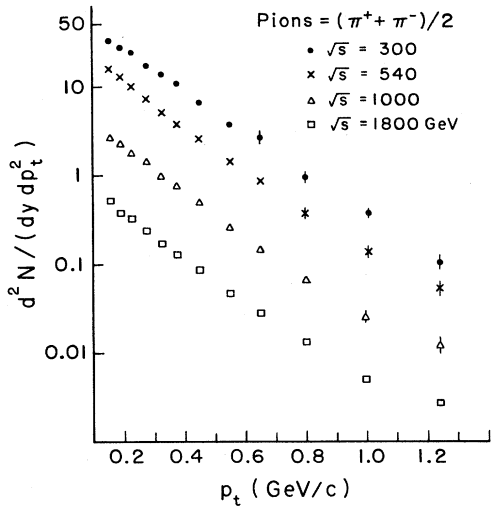

FIG. 10. $d^2N/(dy\,dp_t^2)$ as a function of p_t for pions for four different center-of-mass energies (300, 540, 1000, and 1800 GeV).

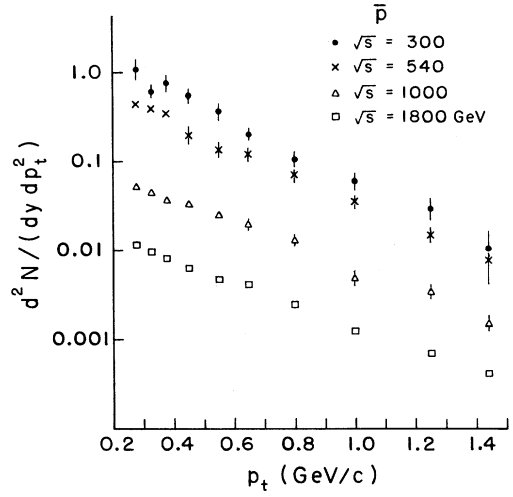

FIG. 12. $d^2N(dy\,dp_t^2)$ as a function of p_t for antiprotons for four different center-of-mass energies (300, 540, 100, and 1800 GeV).

and antiproton data can be fitted with exponentials, $a\exp(-\alpha p_t)$. The pion data cannot be fitted to an exponential form but can be parametrized with a power law [3], $b(p_t+p_0)^{-n}$, with $p_0=1.0$ GeV/c (fixed). We have determined these parameters using p_t intervals, $0.25<p_t<1.5$ GeV/c for the kaon data, $0.35<p_t<1.75$ GeV/c for the antiproton data, and $0.15<p_t<1.5$ GeV/c for the pion data. The lower p_t-cutoff values are dictated by considerations of track curvature in the magnetic field, decays, dE/dx losses, and backgrounds; the upper p_t-cutoff values are dictated by the capability of the TOF system in mass separation.

Using the fitted parameters we have calculated the average transverse momentum, $\langle p_t\rangle$ and the number of particles, N. Integrating the fitted expression from 0 to ∞, we get

$$\langle p_t\rangle = 2/\alpha, \quad N = a/(\alpha^2)\,, \tag{10a}$$

and

$$\langle p_t\rangle = 2p_0/(n-3), \quad N = bp_0^{2-n}/[(n-1)(n-2)]\,, \tag{10b}$$

for exponential and power-law functions, respectively.

In Table I we show $\langle p_t\rangle$ and the ratios K/π for different energies by integrating the fitted expressions from 0 to ∞ [i.e., using Eq. (10)]. These $\langle p_t\rangle$ values are plotted in Fig. 13 as a function of $\sqrt{s}$, along with those for the energy region of the CERN Intersecting Storage Rings (ISR) [18]. The main feature of $\langle p_t\rangle$ dependence on $\sqrt{s}$ is that it increases linearly with $\ln(\sqrt{s})$ for pions, and increases faster than this behavior for kaons and antiprotons—the rate of increase is larger for particles

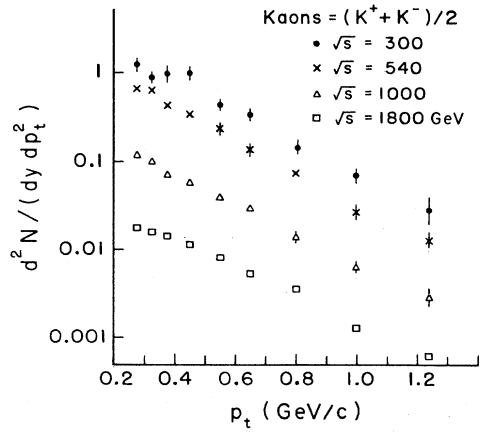

FIG. 11. $d^2N(dy\,dp_t^2)$ as a function of p_t for kaons for four different center-of-mass energies (300, 540, 1000, and 1800 GeV).

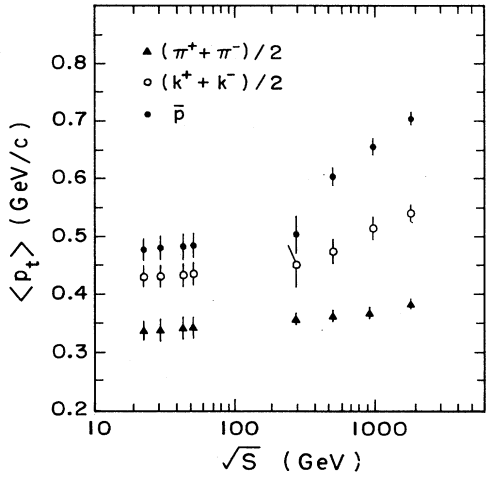

FIG. 13. Plot of $\langle p_t\rangle$ as a function of $\sqrt{s}$; the data for $\sqrt{s}<100$ GeV are from Ref. [18].

with larger mass. The K/π and $\bar{p}/\pi$ ratios as a function of $\sqrt{s}$ are shown in Fig. 14. The data show that there is a definite increase in the ratios from the ISR to the Tevatron energy regime. However, it is not possible to conclude whether the increase is linear in $\ln(\sqrt{s})$ or the ratios have attained constant values at Tevatron energies. The data for the ratios as a function of p_t, for four different energies are shown in Fig. 15, and are tabulated in Tables I(d) and I(e). No definite energy dependence is observed in this figure. As for the p_t dependence, the

TABLE I. (a) Average transverse momentum $\langle p_t \rangle$ in GeV/c and particle ratios for the range, $0.0 < p_t < \infty$ GeV/c, as a function of energy. (b) Average transverse momentum $\langle p_t \rangle$ in GeV/c and particle ratios for the range, $0.0 < p_t < 1.5$ GeV/c, as a function of energy. (c) Comparison of present $\sqrt{s} = 1800$ GeV data [see Table I(b)] with previously published data (Ref. 3) for the p_t interval $0.0 < p_t < 1.5$ GeV/c. (d) Values of k/π ratios (%) as a function of p_t for various values of $\sqrt{s}$. (e) Values of $\bar{p}/\pi$ ratios (%) as a function of p_t for various values of $\sqrt{s}$.

(a)

	$\sqrt{s}=300$ GeV	$\sqrt{s}=540$ GeV	$\sqrt{s}=1000$ GeV	$\sqrt{s}=1800$ GeV
$\langle p_t \rangle_\pi$	0.363±0.006	0.372±0.004	0.372±0.004	0.390±0.004
$\langle p_t \rangle_K$	0.458±0.025	0.482±0.013	0.530±0.012	0.552±0.006
$\langle p_t \rangle_{\bar{p}}$	0.505±0.040	0.606±0.026	0.668±0.025	0.716±0.011
K/π	0.105±0.020	0.112±0.010	0.104±0.008	0.108±0.005
$\bar{p}/\pi$	0.072±0.020	0.078±0.011	0.068±0.008	0.077±0.004

(b)

$\langle p_t \rangle_\pi$	0.341±0.006	0.348±0.004	0.350±0.004	0.361±0.004
$\langle p_t \rangle_K$	0.444±0.025	0.463±0.013	0.499±0.012	0.515±0.006
$\langle p_t \rangle_{\bar{p}}$	0.481±0.040	0.551±0.026	0.587±0.025	0.612±0.011
K/π	0.105±0.020	0.112±0.010	0.103±0.008	0.107±0.005
$\bar{p}/\pi$	0.071±0.020	0.076±0.011	0.065±0.008	0.072±0.004

(c)

	Present data	Previously published data (Ref. [3])
$\langle p_t \rangle_\pi$ (GeV/c)	0.361±0.004	0.362±0.003
$\langle p_t \rangle_K$ (GeV/c)	0.515±0.006	0.51±0.01
$\langle p_t \rangle_{\bar{p}}$ (GeV/c)	0.612±0.010	0.61±0.02
K/π	0.107±0.005	0.112±0.004
$\bar{p}/\pi$	0.072±0.004	0.074±0.006

(d)

p_t interval (GeV/c)	$\sqrt{s}=300$ GeV	$\sqrt{s}=540$ GeV	$\sqrt{s}=1000$ GeV	$\sqrt{s}=1800$ GeV
0.25–0.30	8.1±1.7	9.9±0.9	9.2±0.7	7.8±0.3
0.30–0.35	7.5±1.4	12.7±1.1	10.4±0.7	9.1±0.3
0.35–0.40	9.5±1.6	10.6±0.9	9.3±0.7	9.7±0.3
0.40–0.50	16.1±1.5	13.1±0.7	11.8±0.7	13.9±0.3
0.50–0.60	16.4±2.5	16.9±1.6	15.3±1.2	16.2±0.6
0.60–0.70	17.9±3.5	17.3±1.7	19.8±1.5	18.1±0.7
0.70–0.95	19.4±2.4	20.2±1.4	19.8±1.2	21.6±0.7
0.95–1.15	23.8±4.9	21.2±2.1	25.9±1.9	24.6±0.8
1.15–1.35	25.7±7.5	25.0±3.2	27.8±2.6	25.8±0.9
1.35–1.55		31.2±4.9	32.8±3.9	25.2±1.0

(e)

0.30–0.35	4.5±1.4	8.1±1.5	4.8±0.6	5.5±0.2
0.35–0.40	8.1±1.8	8.8±1.0	5.0±0.6	6.0±0.2
0.40–0.50	8.7±1.3	7.5±0.7	6.8±0.5	7.3±0.2
0.50–0.60	9.4±3.0	9.7±1.5	9.8±1.2	10.0±0.6
0.60–0.70	10.1±3.5	15.0±2.1	12.9±1.5	14.6±0.8
0.70–0.95	10.6±2.6	18.3±1.8	18.2±1.4	19.1±0.8
0.95–1.15	21.4±6.1	25.2±3.1	20.3±2.2	23.5±1.0
1.15–1.35	31.7±11.2	27.8±4.7	31.2±3.6	30.4±1.3
1.35–1.55		33.2±7.0	34.6±5.2	34.7±1.6
1.55–1.75			36.2±7.0	35.3±1.8

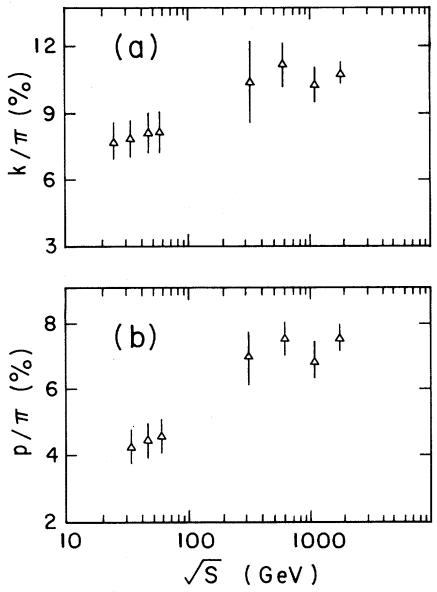

FIG. 14. Plot of $\bar{p}/\pi$ and K/π ratios as a function of $\sqrt{s}$; the data for $\sqrt{s} < 100$ GeV are from Ref. [18]. The π and K data are averaged over positive and negative particles.

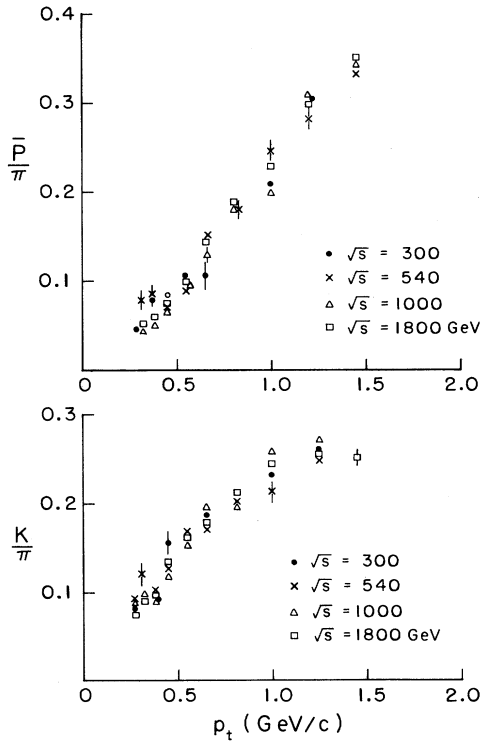

FIG. 15. The ratios $\bar{p}/\pi$ and K/π as a function of p_t for four center-of-mass energies (300, 540, 1000, and 1800 GeV). The π and K data are averaged over positive and negative particles. For clarity, error bars are not shown for all data; the data shown without error have about the same errors as shown for the other data.

$\bar{p}/\pi$ ratio seems to increase monotonically with p_t; the K/π shows a trend of flattening out at a value of ~ 0.25 for $p_t > 0.9$ GeV/c.

In a previous publication [3] we have compared our $\pi^{\pm}$, $K^{\pm}$, $\bar{p}$ production data at $\sqrt{s} = 1800$ GeV with other high-energy data: charged particle data from UA2 [19] experiment at $\sqrt{s} = 540$ GeV, and K_S^0 data from UA5 [20] at $\sqrt{s} = 200$, 546, and 900 GeV. These data as well as K_s^0 production data of CDF [21] at $\sqrt{s} = 630$ and 1800 GeV show the same trend in energy dependence as discussed in the previous section.

In Ref. [3], we have reported $\langle p_t \rangle$ and particle ratio values integrating the fitted expressions for $0.0 < p_t < 1.5$ GeV/c at $\sqrt{s} = 1800$ GeV. We also present here these values for the new data in Table I(b), which are compared with the published data of Ref. [3] in Table I(c). As can be seen in the table the present data are in good agreement with our previously published values.

B. Multiplicity dependence

In this section we deal with the correlation of $\langle p_t \rangle$ and particle ratios as a function of charged particle multiplicity density $dN_c/d\eta$. We present here only the $\sqrt{s} = 1800$ GeV data, as the experiment was run to study this topic at the highest available energy to collect data with high statistics to determine $\langle p_t \rangle$ and particle ratios accurately as a function charged multiplicity. We have paid special attention in evaluating the contribution of systematic errors in the data analysis. The systematic er-

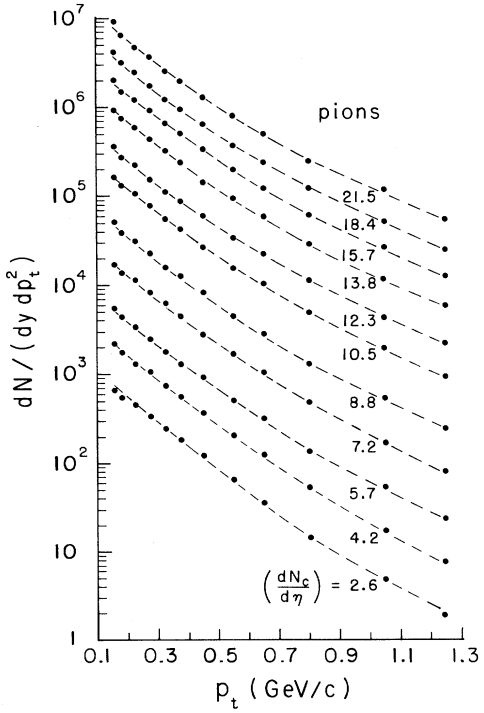

FIG. 16. $d^2N(dy\,dp_t^2)$ as a function of p_t for pions for 11 different values of particle densities $dN_c/d\eta$. The ordinate scale is arbitrary and the data for various $dN_c/d\eta$ have been scaled for the purpose of display.

rors are related to the estimate of background as well as on the evaluation of correction factors based on Monte Carlo calculations. As mentioned in Sec. VI, other independent analyses have been performed to estimate the systematic effects in $\langle p_t \rangle$ and particle ratio values. We find that the systematic errors are more important than the statistical errors, as shown in Tables II(a) and II(b). Except for the highest multiplicity bin, the bins have been chosen such that the number of tracks in each multiplicity bin is approximately equal. As a result, the statistical errors shown in Tables II(a) and II(b) are independent of $dN_c/d\eta$. The systematic errors increase with increasing multiplicity from a few MeV/c at low multiplicity to a value of 20 MeV/c at the highest bin. The values shown in the tables correspond to the highest estimated value.

The particle density $dN_c/d\eta$ is obtained by dividing N_c, the number of charged particles associated with the multiplicity hodoscope by 6.5, the pseudoparity interval accepted by the hodoscope. (Monte Carlo studies have shown that this procedure yields the correct rapidity particle density within 10%.)

The p_t distributions for various charged particle densities using data for a fixed N_c interval are obtained in the same way as described in the previous section. In Figs. 16–18 we present the p_t distributions for pions, kaons, and antiprotons for eleven different $dN_c/d\eta$ values (2.6–21.5). The dashed curves shown in these figures correspond to fits discussed in the previous section. Using the fitted parameters, we have evaluated the $\langle p_t \rangle$ values and the particle ratios for the p_t interval $0.0 < p_t < \infty$. The values of $\langle p_t \rangle$ are listed in Table II(a), and the particle ratios in Table II(b). The values shown in these tables are plotted in Fig. 19, as a function of $dN_c/d\eta$.

Previously published results [3] of $\langle p_t \rangle$ values using data from an earlier run were obtained in the p_t interval $0.0 < p_t < 1.5$ GeV/c; in order to compare the new data with the published data, we have evaluated $\langle p_t \rangle$ and particle ratios for $0.0 < p_t < 1.5$ GeV/c for the new data. We note that apart from better statistics, the acceptance corrections for the present data have been studied in more details and with better accuracy; also, the present data extend to higher values of $dN_c/d\eta$. The new data agree with the previously published data when the systematic errors are taken into account. However, we mention here that some trends in the behavior of kaon production shown by the previous data [3] are not confirmed by the present data. The trend of the rise of K/π ratio at

TABLE II. (a) Values of $\langle p_t \rangle$ in GeV/c as a function of $dN_c/d\eta$ for $0 < p_t < \infty$ along with statistical and systematic errors. (b) Values of particle ratios for $0 < p_t < \infty$ as a function of $dN_c/d\eta$, along with statistical and systematic errors.

(a)

$dN_c/d\eta$	$\langle p_t \rangle_\eta$	$\langle p_t \rangle_K$	$\langle p_t \rangle_{\bar{p}}$
1.1	0.333±0.001±0.020	0.452±0.003±0.020	0.530±0.005±0.020
2.6	0.353±0.001±0.020	0.487±0.003±0.020	0.574±0.005±0.020
4.2	0.370±0.001±0.020	0.507±0.003±0.020	0.647±0.005±0.020
5.7	0.391±0.001±0.002	0.558±0.003±0.020	0.704±0.005±0.020
7.2	0.403±0.001±0.020	0.571±0.003±0.020	0.734±0.005±0.020
8.8	0.413±0.001±0.020	0.604±0.003±0.020	0.769±0.005±0.020
10.5	0.423±0.001±0.020	0.652±0.003±0.020	0.792±0.005±0.020
12.3	0.434±0.001±0.020	0.659±0.003±0.020	0.824±0.005±0.020
13.8	0.440±0.001±0.020	0.696±0.003±0.020	0.858±0.005±0.020
15.7	0.446±0.001±0.020	0.747±0.003±0.020	0.872±0.005±0.020
18.4	0.448±0.001±0.020	0.760±0.003±0.020	0.951±0.005±0.020
21.5	0.454±0.001±0.020	0.791±0.003±0.020	0.990±0.005±0.020
25.4	0.472±0.002±0.020	0.820±0.006±0.020	1.020±0.010±0.020

(b)

$dN_c/d\eta$	K/π	$\bar{p}/\pi$
1.1	0.096±0.001±0.005	0.055±0.002±0.005
2.6	0.106±0.001±0.005	0.072±0.002±0.005
4.2	0.107±0.001±0.005	0.077±0.002±0.005
5.7	0.108±0.001±0.005	0.076±0.002±0.005
7.2	0.109±0.001±0.005	0.081±0.002±0.005
8.8	0.112±0.001±0.005	0.081±0.002±0.005
10.5	0.108±0.001±0.005	0.079±0.002±0.005
12.3	0.110±0.001±0.005	0.077±0.002±0.005
13.8	0.113±0.001±0.005	0.078±0.002±0.005
15.7	0.110±0.001±0.005	0.080±0.002±0.005
18.4	0.103±0.001±0.005	0.083±0.002±0.005
21.5	0.103±0.001±0.005	0.078±0.002±0.005
25.4	0.103±0.003±0.005	0.088±0.004±0.005

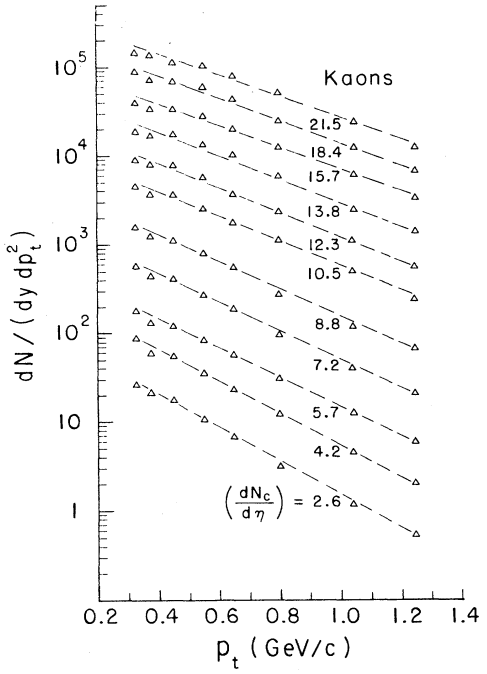

FIG. 17. $d^2N(dy\,dp_t^2)$ as a function of p_t for kaons for 11 different $dN_c/d\eta$ values. The data for various $dN_c/d\eta$ have been scaled by the same factors as in Fig. 16.

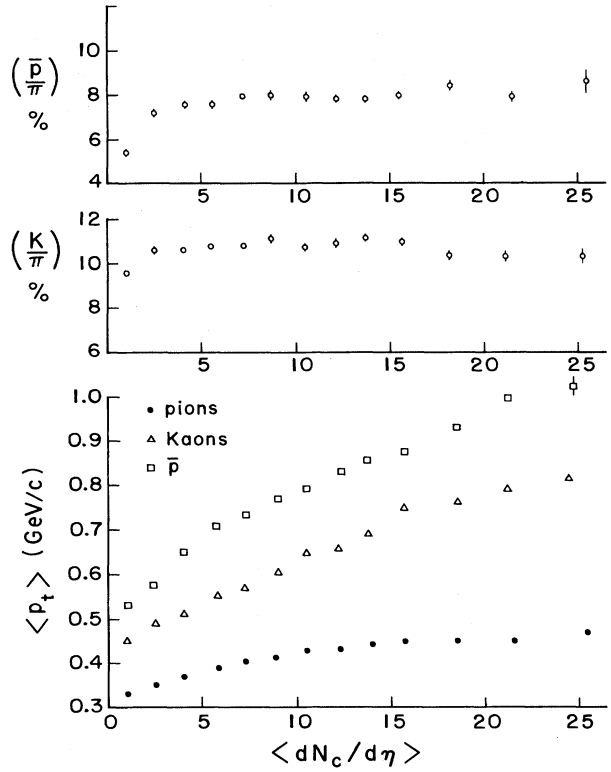

FIG. 19. Average transverse momentum, $\langle p_t \rangle$ and K/π and $\bar{p}/\pi$ ratios as a function of charged particle density ($dN_c/d\eta$). Systematic errors are not shown in the figure but given in Tables II(a) and II(b).

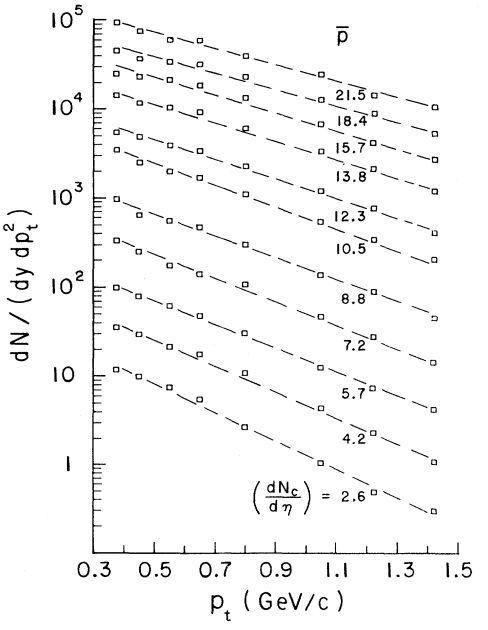

FIG. 18. $d^2N(dy\,dp_t^2)$ as a function of p_t for antiprotons for 11 different $dN_c/d\eta$ values. The data for various $dN_c/d\eta$ have been scaled by the same factors as in Fig. 16.

high multiplicity as well as the apparent flattening of $\langle p_t \rangle$ for kaons with the increase of multiplicity are not seen in the new data.

VIII. SUMMARY AND CONCLUSIONS

We have studied the production of centrally produced $\pi^{\pm}$, $K^{\pm}$, and $p^{\pm}$ at the Fermilab collider as a function of center-of-mass energies, $\sqrt{s}=300$, 540, 1000, and 1800 GeV. From transverse momentum distributions we have evaluated the average transverse momentum, $\langle p_t \rangle$ and the ratios K/π and $\bar{p}/\pi$.

We find that the variation of $\langle p_t \rangle$ with the center-of-mass energy depends on the particle type. For pions, the $\langle p_t \rangle$ shows a linear rise in $\ln(\sqrt{s})$ from the energies reached at the ISR. For kaons and antiprotons (protons), the increase is much faster than a linear $\ln(\sqrt{s})$ dependence [see Fig. 13 and Table I(a)]. The particle ratios are not strongly dependent on $\sqrt{s}$; comparing these data with lower "ISR" energies, both K/π and $\bar{p}/\pi$ ratios seem to increase slowly with $\ln(\sqrt{s})$ as can be seen in Fig. 14. At collider energies, the ratios as a function of p_t are essentially the same for all energies (see Fig. 15), the $\bar{p}/\pi$ ratio rising monotonically with p_t and the K/π ratio tending to a plateau at high p_t.

The study of particle production as a function of charged particle density ($dN_c/d\eta$) from the $\sqrt{s}=1800$ GeV data has been extended to a higher value of $dN_c/d\eta$ (up to ~ 25). Higher statistics data presented here confirm the trends reported in our earlier publication [3] that the increase of $\langle p_t \rangle$ with ($dN_c/d\eta$) depends on the mass of the particle (see Fig. 19). The dependence of $\langle p_t \rangle$ on charged particle density has been of current interest [22–24]. Wang and co-workers [22] have presented detailed calculations to explain the phenomenon in terms of the "mini-jet" model. This effect has also been associated with the presence of transverse flow of the hadronic matter [23,24], and might be indicative of the formation of the quark-gluon plasma.

ACKNOWLEDGMENTS

We thank the administrative and technical staff at Fermilab and our respective universities for their support of the experiment. This work was supported in part by the U.S. Department of Energy, the National Science Foundation, and the Jesse Jones Faculty Equipment Fund at Notre Dame.

[1] L. Van Hove, Phys. Lett. **118B**, 138 (1982); L. D. McLerrand and B. Svetitsky, *ibid.* **98B**, 195 (1981); J. Kuti, J. Polonyi, and K. Szlchanyi, *ibid.* **98B**, 199 (1981); J. Kogut *et al.*, Phys. Rev. Lett. **51**, 869 (1983).

[2] T. Alexopoulos *et al.*, Phys. Rev. Lett. **60**, 1622 (1988); S. Banerjee *et al.*, *ibid.* **62**, 12 (1989).

[3] T. Alexopoulos *et al.*, Phys. Rev. Lett. **64**, 991 (1990).

[4] J. D. Bjorken, Phys. Rev. D **27**, 140 (1983). The energy density ε_0 is calculated from $\varepsilon_0=\frac{3}{2}(dN_c/d\eta)(\langle e_t \rangle/\pi r^2\tau)$, using transverse energy $\langle e_t \rangle=0.4$ GeV, and 1 fm for both radius r and lifetime τ.

[5] T. Alexopoulos *et al.*, Phys. Rev. D **46**, 2773 (1992).

[6] C. Allen *et al.*, Nucl. Instrum. Methods A **294**, 108 (1990).

[7] E. W. Anderson *et al.*, Nucl. Instrum. Methods A **295**, 86 (1990).

[8] S. H. Oh *et al.*, Nucl. Instrum. Methods A **303**, 277 (1991).

[9] T. Alexopoulos *et al.*, Nucl. Instrum. Methods A **311**, 156 (1992).

[10] S. Banerjee *et al.*, Nucl. Instrum. Methods A **269**, 121 (1988).

[11] P. Cole, Ph.D. thesis, Purdue University, 1991; C. Allen, thesis, Purdue University, 1991.

[12] T. Alexopoulos, Ph.D. thesis, University of Wisconsin, 1991.

[13] C. H. Wang, Ph.D. thesis, Iowa State University, 1991.

[14] Y. Zhan, Ph.D. thesis, University of Notre Dame, 1991.

[15] G. J. Alner *et al.*, Nucl. Phys. **B291**, 475 (1987).

[16] F. Paige and S. D. Protopopescu, Brookhaven National Laboratory, Technical Report No. BNL 38034, 1986 (unpublished).

[17] T. Sjöstrand, Comput. Phys. Commun. **39**, 347 (1986).

[18] B. Alper *et al.*, Nucl. Phys. **B87**, 19 (1975); **B100**, 237 (1975); T. Akesson *et al.*, Phys. Lett. **108B**, 58 (1982); G. Arnison *et al.*, *ibid.* **118B**, 167 (1982).

[19] M. Banner *et al.*, Phys. Lett. **122B**, 322 (1983); M. Banner *et al.*, Z. Phys. C **27**, 329 (1985).

[20] K. Alpgard *et al.*, Phys. Lett. **115B**, 65 (1982); G. J. Alner *et al.*, Nucl. Phys. **B258**, 505 (1985); R. E. Ansorge *et al.*, Z. Phys. C **41**, 179 (1988).

[21] F. Abe *et al.*, Phys. Rev. D **40**, 3791 (1989).

[22] X. N. Wang and R. C. Hwa, Phys. Rev. D **39**, 187 (1989); X. N. Wang and M. Gyulassy, *ibid.* **45**, 844 (1992), and references cited therein; X. N. Wang and M. Gyulassy, Phys. Lett. B **282**, 466 (1992).

[23] E735 Collaboration, T. Alexopoulos *et al.*, *in Proceedings of the 7th Winter Workshop on Nuclear Dynamics,* edited by W. Baer and J. Kapusta (World Scientific, Singapore, 1991), p. 248; G. Bersch *et al.*, Phys. Rev. D **37**, 1202 (1988), and the references cited therein.

[24] P. Levai and B. Müller, Phys. Rev. Lett. **67**, 1519 (1991).